RSC Advances

PAPER

View Article Online
View Journal | View Issue

Cite this: *RSC Adv.*, 2014, **4**, 4796

An airflow-controlled solvent evaporation route to hollow microspheres and colloidosomes†

Conghui Yuan,[a] Birong Zeng,[a] Shirong Yu,[a] Jie Mao,[a] Xiaoling Chen,*[b] Weiang Luo,[a] Yiting Xu,[a] Feng-Chih Chang[c] and Lizong Dai*[a]

Received 11th October 2013
Accepted 10th December 2013

DOI: 10.1039/c3ra45758c

www.rsc.org/advances

A facile and large-scale method combining airflow-controlled solvent evaporation and amphiphilic copolymer self-assembly has been developed for the generation of hollow polymer microspheres, colloidosomes or even organic–inorganic hybrid colloidosomes. By replacing traditional agitation with the controllable airflow, this surfactant free route showed promising prospect in the fabrication of microcapsules with closed pore morphology. While the hollow polymer microspheres had an adjustable pore structure, the polymer colloidosomes and the hybrid colloidosomes possessed seamless surfaces, making them suitable for the stable encapsulation of small molecules. The hybrid colloidosomes constructed from polymer and Fe_3O_4 nanoparticles, and the ternary hybrid colloidosomes derived from polymer, polymer nanospheres and Fe_3O_4 nanoparticles displayed superparamagnetic properties and were excellent contrast agents for magnetic resonance imaging. More importantly, both hybrid colloidosomes and ternary hybrid colloidosomes exhibited a significant evolution of pore morphology from a closed pore structure to an open pore structure in response to the temperature variation, which induced a controllable release of guest molecules.

1. Introduction

Polymeric microcapsules with well-defined hollow or porous structures such as vesicles,[1–3] polymersomes[4–6] and colloidosomes[7–10] are unique supporting materials for drug or catalyst loading, due to their huge interior cavity and high specific surface area. The control of pore morphology is critical but yet a challenge. To achieve a stable encapsulation or loading of guests, a closed pore structure is promising. Nevertheless, traditional methods including solvent evaporation,[11–13] template assisted methods[14–16] and solvent swelling[17,18] always lead to open pore morphology, though these methods are simple and suitable for large-scale fabrication. Recently, self-assembly[19–21] and microfluidics[22–25] methods have emerged as effective routes to the controllable formation of polymer microspheres with closed pore structure. However, challenges remain in design and synthesis of functional copolymers which are suitable for these two methods. Herein, we develop a facile and large-scale method namely airflow-controlled solvent evaporation, which leads to the formation of porous microspheres, colloidosomes and organic–inorganic hybrid colloidosomes with closed pore structure and controllable pore morphology.

Our approach started from a poly(styrene-*co*-octadecyl poly(ethylene glycol)-600-butenedioate) (P(St-*co*-O-B-EG600)) core–shell nanoparticle, which was prepared by miniemulsion copolymerization of styrene (St) and amphiphilic oligomer named octadecyl poly(ethylene glycol)-600-butenedioate (O-B-EG600).[9,26,27] This nanosphere comprised a hydrophobic PSt core and a hydrophilic P(O-B-EG600) shell. Since the core–shell nanospheres were non-crosslinked or partially-crosslinked, they could be completely or partially dissolved in dichloromethane (DCM), thus forming an amphiphilic random copolymer solution. By simply dispersing this random copolymer solution in water system under the driving force of airflow, hollow or porous polymer microspheres were formed (Scheme 1 and 1S†). We envisaged the possibility of controlling the organic solvent evaporation rate, in combination with the self-assembly of amphiphilic random copolymer on the oil–water interface, to generate hollow polymer microspheres with closed pore structure. We also tested the feasibility of this method to fabricate colloidosomes and organic–inorganic hybrid colloidosomes possessing closed pore morphology.

[a]*Department of Materials Science and Engineering, College of Materials, Xiamen University, Xiamen, China. E-mail: lzdai@xmu.edu.cn; Fax: +86-592-2183937; Tel: +86-592-2186178*

[b]*Department of Endodontics, Xiamen Stomatology Hospital, Teaching Hospital of Fujian Medical University, Xiamen 361003, China. E-mail: tinachen0628@163.com*

[c]*Department of Materials and Optoelectronic Science, National Sun Yat-Sen University, Kaohsiung, Taiwan 804*

† Electronic supplementary information (ESI) available: SEM and TEM images of P(St-*co*-O-B-EG600) nanospheres; magnetic properties of Fe_3O_4 nanoparticles and hybrid colloidosomes; pyrene controlled release data. See DOI: 10.1039/c3ra45758c

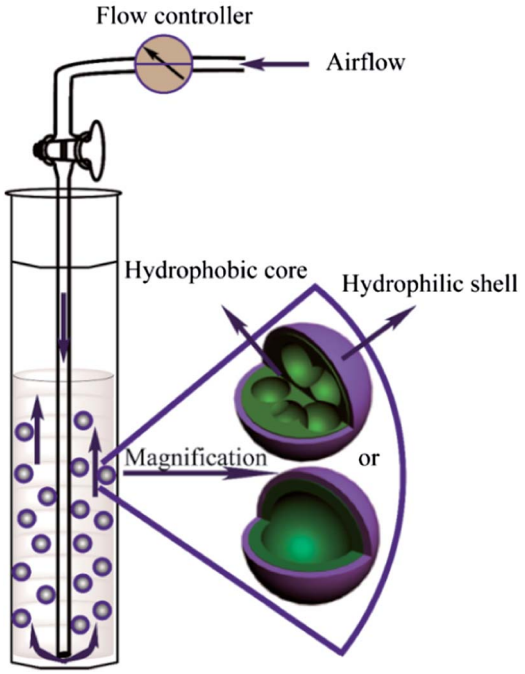

Scheme 1 Preparation equipment and formation process of hollow or porous microspheres with closed pore structure.

2. Experimental section

2.1 Materials

St and divinylbenzene (DVB) were purchased from Aldrich. Azoisobutyronitrile (AIBN) was supplied by Alfa Aesar and recrystallized from methanol before use. Pyrene and *N*,*N*′-methylene bisacrylamide (MBA) were analytical grade and were used as received from Shanghai Chemical Reagent Industry. O-B-EG600 was synthesized by using a previously reported route.[26] The preparation of P(St-*co*-O-B-EG600) core–shell nanoparticle was reported in our previously work.[9,27] Magnetic Fe_3O_4 nanoparticles were prepared according to a reported procedure.[28]

2.2 Preparation procedure

P(St-*co*-O-B-EG600) hollow microspheres. Uncrosslinked P(St-*co*-O-B-EG600) core–shell nanospheres were dissolved in DCM to form a 20.0 wt% polymer solution. A special long reaction tube (50.0 cm high and 1.0 cm radius) assembled with a gas duct was used as a reactor (Scheme 1). The gas duct stretched to the bottom of the reaction tube. The distance between the gas duct nozzle and the tube bottom was fixed to be 0.2 cm. 20.0 mL of polymer solution followed by 100.0 mL deionized water was added into the reactor. Then, different airflow rates such as 2.0, 4.0 and 8.0 L min^{-1} were adopted to break up the polymer solution. After 10.0 min treatment, the mixture was filtered and solid hollow microspheres were obtained.

Polymer–polymer nanosphere colloidosomes. In this preparation experiment, we used P(St-*co*-O-B-EG600) nanospheres with shell crosslinked structure (water soluble MBA was used as crosslinker). Consequently, the nanosphere core was soluble in DCM, while the nanosphere shell was not. After dispersing the shell crosslinked nanospheres in DCM to form a 20.0 wt% suspension solution, the polymer–polymer nanosphere colloidosomes were constructed by using the same method as the preparation of P(St-*co*-O-B-EG600) hollow microspheres (airflow rate: 4.0 L min^{-1}).

Polymer–Fe_3O_4 nanoparticle hybrid colloidosomes. To a 20.0 wt% P(St-*co*-O-B-EG600) polymer DCM solution was added oleic acid decorated hydrophobic Fe_3O_4 nanoparticles (15.0 wt % of the solid content). The mixture was sonicated for 30 min to ensure the complete dispersion of Fe_3O_4 nanoparticles in the polymer matrix. The hybrid colloidosomes were prepared by using the same method which was used to fabricate P(St-*co*-O-B-EG600) hollow microspheres (airflow rates such as 2.0, 4.0 and 8.0 L min^{-1} were used).

Polymer–polymer nanosphere–Fe_3O_4 nanoparticle ternary hybrid colloidosomes. In this preparation procedure, the P(St-*co*-O-B-EG600) nanospheres were core crosslinked by using a hydrophobic crosslinker DVB. P(St-*co*-O-B-EG600) nanospheres crosslinked with 5.0 and 10.0 wt% of DVB were dispersed in DCM to form a 20.0 wt% solution. After 30.0 min sonication, Fe_3O_4 nanoparticles (15.0 wt% of the solid content) were added. The mixture was sonicated for additional 30.0 min. The hybrid colloidosomes were then prepared according to the method which was used for the fabrication hybrid colloidosomes (airflow rate: 4.0 L min^{-1}).

Encapsulation of pyrene in hybrid colloidosomes. In this preparation procedure, DCM was replaced by a pyrene DCM solution with a concentration 1.0 wt%. Then the hybrid colloidosomes were prepared according to the former methods.

2.3 Characterization

To obtain microscope images of the resultant products, samples were deposited on the surface of glass sheets. The samples were gold sputtering treated, and field emission scanning electron microscope (FE-SEM, LEO-1530) was used to observe the surface morphology of the resultant products.

Transmission electron microscopy (TEM) measurement was performed with a JEM2100 at an acceleration voltage of 200 kV. To prepare the TEM samples, a small drop of resultant product aqueous dispersion was deposited onto a carbon-coated copper electron microscopy (EM) grid and then dried at room temperature. The energy dispersion spectroscopy analysis was also carried out on an energy dispersive spectrdmeter (ZNCA Energy TEM 100 X-ray energy spectrum) assembled on JEM2100.

Optical microscope was also used to observe the morphology of the hollow microspheres and colloidosomes. Samples were deposited on microscope slides and measured by Metallurgical Microscope (ECLIPSE ME600L). The particle size of the microspheres were tested by using a LOP-III OMC laser particle size analyzer. DC magnetization measurements were performed by using a Quantum Design SQUID magnetometer. T_2 weighted imaging experiments were performed on a 7 T (299.8 MHz)/160 mm bore varian magnetic resonance imaging (MRI) system

(Agilent Technologies, Santa Clara, Ca, USA) using a quadraure-coil probe with a maximum FOV of 65 × 65 × 80 mm^3 under extremely homogeneous field. The maximum gradient strength acting on three axes was 400 mT m^{-1}.

Fluorescence microscope images of pyrene encapsulated in hybrid colloidosomes were obtained from an inverted fluorescence microscope (LeicaDMLL). Samples in aqueous dispersion were dropped onto microscope slides and dried at room temperature before observation. Fluorescence emission spectra of pyrene were measured by fluorescence spectrophotometry on HITACHI F-7000 at predetermined temperatures (stimulation slit width: 3 nm, emission slit width: 3 nm, scanning speed: 60 nm min^{-1}).

3. Results and discussion

3.1 Hollow microspheres and colloidosomes

The solvent evaporation method has been widely applied in the fabrication of hollow microspheres. However, the excessive use of surfactants and vigorous stirring during the formation of microspheres not only bring problems to the purification of product, but also result in an open pore structure. In our airflow-controlled solvent evaporation route, the amphiphilic random copolymer derived from the core–shell nanoparticles can self-emulsify the polymer–DCM–water system, thus stabilizing the polymer–DCM droplets in water. Moreover, this approach adopts an airflow method instead of vigorous stirring to break up polymer–DCM solution into micro-droplets and promote the evaporation of DCM, which leads to the formation of closed pore structure. The preparation route is illustrated in Scheme 1. The particularly long reaction tube was used to improve the contacting time between airflow and polymer droplets, therefore increasing the evaporation speed of DCM. We anticipated this approach would be a simple, green and large-scale method to construct hollow microspheres and colloidosomes. During the experimental process, we observed that the concentration of polymer and the ratio between water and DCM were essential in the formation of microspheres with promising size and closed pore structure. Polymer in DCM solution with concentrations higher and lower than 20 wt% could result in extremely large size and open pore structure, respectively. To ensure the complete evaporation of DCM from interior microspheres, the volume ratio between water and DCM should be higher than 5 : 1.

Uncrosslinked P(St-*co*-O-B-EG600) core–shell nanospheres (Fig. 1S†) were firstly used as amphiphilic random copolymer source to fabricate hollow microspheres. Since the DCM evaporation and the formation of hollow microspheres were assisted by the airflow, we envisaged that the pore structure in interior of the microspheres could be controlled by the airflow rate. We found that the surface of the as prepared P(St-*co*-O-B-EG600) microspheres were composed of a lot of dark domains (Fig. 1A and B). Because the brightness of materials observed by SEM depended on the electron emission rate, thin domains would be darker than thick domains. We envisioned that the dark domains represented the pores embedded in the microspheres. TEM was then used to confirm the interior structure of the

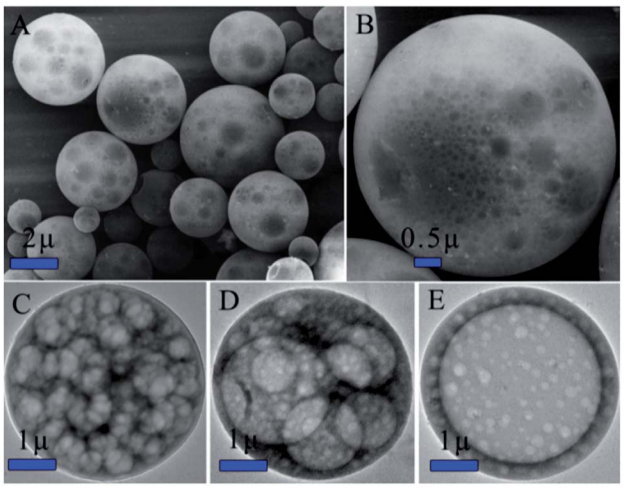

Fig. 1 Overview (A) and magnified (B) SEM images of P(St-*co*-O-B-EG600) hollow microspheres; (C), (D) and (E) are the TEM images of the P(St-*co*-O-B-EG600) hollow microspheres prepared from 2.0, 4.0 and 8.0 L min^{-1} airflow rate, respectively.

microspheres. As shown in Fig. 1C–E, pores with various sizes were buried under the shells. Interestingly, we observed that the pore morphology of the microspheres exhibited an evident evolution as the change of airflow rate. The pore size increased with the increasing of airflow rate, therefore a hollow structure with small pores embedded in the shell was observed to the microspheres prepared by using 8.0 L min^{-1} airflow rate. Thus, it is reasonable to believe that this airflow-controlled solvent evaporation route is an effective method to generate hollow microspheres with closed pore structure. We also noted that microspheres obtained from a low airflow rate (such as 1.0 L min^{-1}) possessed extremely large diameter (>20.0 μm) and wide size distribution (Fig. 2S†). However, the average diameters of microspheres prepared by using airflow rate ≥2.0 L min^{-1} were around 10.0 μm and depended less on the increase of airflow rate (Fig. 2S†). Therefore, airflow rates ≥2.0 L min^{-1} were adopted to fabricate the microcapsules. Importantly, it should be noted that all these microspheres showed high polydispersities, indicating that this airflow-controlled solvent evaporation method was not effective in the preparation of monodispersed microspheres.

Since our approach was surfactant free, it was important to understand how the polymer droplets stabilized themselves during the formation of hollow microspheres. We envisioned that the P(O-B-EG600) polymer chains played a key role in the stabilization of polymer droplets. In the formation process of the hollow microspheres, the polymer–DCM mixture was firstly broken up into micro-droplets by the high speed airflow. Then the hydrophilic P(O-B-EG600) polymer chains moved to the surface of polymer droplets, while the hydrophobic PSt chains migrated into the core of the polymer droplets. If this were the case, we would expect that a hollow microsphere was composed of a hydrophilic P(O-B-EG600) outer layer and a hydrophobic PSt inner layer (Scheme 1). However, it was hard to distinguish the P(O-B-EG600) component from the PSt component in the TEM images (Fig. 1C–E), because the hollow microspheres were

too large. To overcome this drawback, we used shell-crosslinked P(St-*co*-O-B-EG600) nanospheres to generate hollow microspheres. As the nanopsphere shell was crosslinked, the PSt core rather than the P(O-B-EG600) shell could be dissolved by DCM. Therefore, after the dispersion of nanospheres in DCM, the as-obtained mixture comprised both PSt polymer chains and undissolved P(O-B-EG600) nanoparticles (Fig. 3S†). If the hollow microspheres were stabilized by the P(O-B-EG600) component, P(O-B-EG600) nanoparticles should be deposited on the surface of the hollow microspheres. Indeed, this was true. As shown in Fig. 2A and B, the obtained microspheres were coated with deformed P(O-B-EG600) nanoparticles. We also observed that some microspheres were not completely covered with P(O-B-EG600) nanoparticles, thus showing a smooth surface (Fig. 2C). This result indicated that the hydrophobic PSt component was embedded in the microspheres. More importantly, a typical SEM image illustrated in Fig. 2D showed a hollow structure, which revealed that the as-prepared microspheres were hollow. To this end, we can confirm that the hollow microspheres are stabilized by the P(O-B-EG600) component. Because these microspheres consist of polymer and polymer nanospheres, we name them as polymer–polymer nanosphere colloidosomes. On the other hand, we can conclude that this airflow-controlled solvent evaporation route is suitable for the fabrication of colloidosomes.

3.2 Organic–inorganic hybrid colloidosomes

We then applied this method to an organic–inorganic hybrid system. Uncrosslinked P(St-*co*-O-B-EG600) nanoparticles accompanied with Fe_3O_4 nanoparticles were dispersed in DCM to form an dispersion with both amphiphilic copolymer and inorganic nanoparticles. We indeed found that our approach could be used to fabricate polymer–Fe_3O_4 nanoparticle hybrid colloidosomes (Fig. 3A and B and 4S†). The surface of these colloidosomes was smooth and contained some dark domains, indicating hollow structures were embedded in interior of the colloidosomes. The hollow structure of these hybrid colloidosomes was also confirmed by TEM. As shown in Fig. 3C–E, the pore structure evolution of hybrid colloidosomes was almost the same with that of the P(St-*co*-O-B-EG600) hollow microspheres. The pore size increased significantly with the improvement of the airflow rate. Hybrid colloidosomes prepared from 2.0 and 4.0 L min^{-1} airflow rate showed a closed pore structure, while that prepared from 8.0 L min^{-1} airflow rate exhibited a hollow structure.

In the magnified SEM image (Fig. 3B), we found that a few Fe_3O_4 nanoparticles were deposited on the colloidosome surface. However, we observed from the TEM images (Fig. 3C–E) that some deep dark domains were dispersed in interior of the hybrid colloidosomes. A high resolution TEM image illustrated in Fig. 3F affirmed that these dark domains were composed of a large amount of Fe_3O_4 nanoparticles. Since the colloidosome was constructed by a P(O-B-EG600) outer layer and a PSt inner layer, it was understandable that the hydrophobic Fe_3O_4 nanoparticles tended to be embedded in the PSt layer.

Since our approach was effective in the generation of polymer–polymer nanosphere and polymer–Fe_3O_4 nanoparticle colloidosomes, we then intended to extend this method to a more complicated system, which possessed polymer, polymer nanospheres and Fe_3O_4 nanoparticles. We expected to obtain a polymer–polymer nanosphere–Fe_3O_4 nanoparticle ternary hybrid colloidosome. Firstly, shell crosslinked P(St-*co*-O-B-EG600) nanospheres were adopted to fabricate this ternary hybrid colloidosome. However, we were failed to obtain hybrid colloidosomes with well defined structures, because the P(O-B-EG600) nanoparticles could not stabilize the PSt-Fe_3O_4 nanoparticle droplets well, thus resulting in an open pore structure (Fig. 5S†). Interestingly, if core crosslinked P(St-*co*-O-B-EG600)

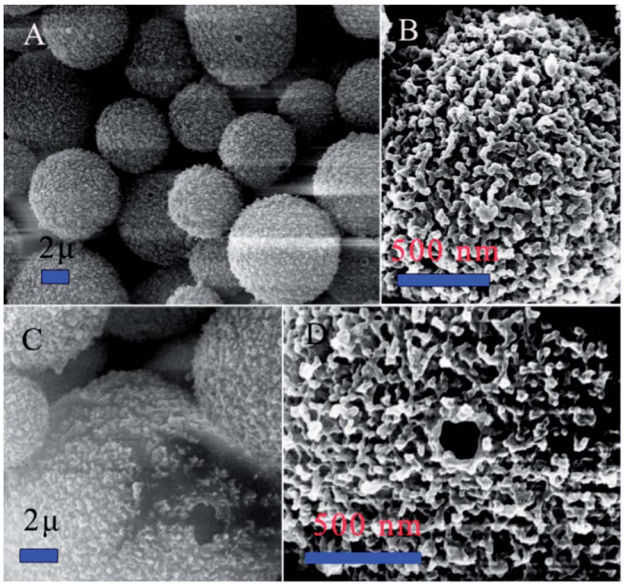

Fig. 2 Overview (A) and magnified (B) SEM images of polymer–polymer nanoparticle colloidosomes; (C) is a typical SEM images of colloidosomes, which were not completely covered by P(O-B-EG600) nanoparticles; (D) colloidosomes with broken hollow structure.

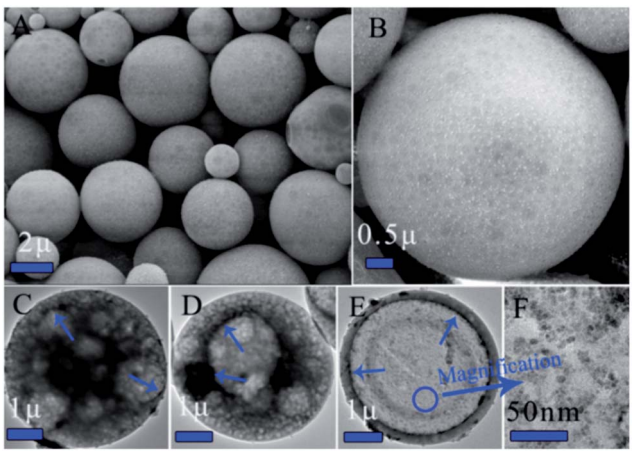

Fig. 3 Overview (A) and magnified (B) SEM images of polymer–Fe_3O_4 nanoparticle hybrid colloidosomes; (C), (D) and (E) are the TEM images of the polymer–Fe_3O_4 nanoparticle hybrid colloidosomes prepared from 2.0, 4.0 and 8.0 L min^{-1} airflow rate, respectively; (F) is a magnified TEM image of the area in (E).

nanoparticles were applied, ternary hybrid colloidosome with closed pore structure could be easily prepared. Fig. 4A and B are the SEM images of ternary hybrid colloidosomes prepared from P(St-*co*-O-B-EG600) nanospheres with different crosslinking percentages, from which we can observe microspheres with dark domains on the surface. A comparison between Fig. 4A and B reveals that the ternary hybrid colloidosomes prepared with higher crosslinked P(St-*co*-O-B-EG600) nanospheres have more smooth surface. We speculate that a higher content of PSt nanospheres in combination with the amphiphilic P(O-B-EG600) polymer chains can emulsify the polymer–polymer nanosphere–Fe_3O_4 nanoparticle droplets better.

Fig. 4C and D illustrate the magnified SEM images of ternary hybrid colloidosomes prepared with P(St-*co*-O-B-EG600) nanospheres crosslinked by 5.0 and 10.0 wt% DVB, respectively. Both of these two colloidosomes showed a polymer–polymer nanosphere–Fe_3O_4 nanoparticle blending surface. Especially, the surface of ternary hybrid colloidosomes prepared by using 10.0 wt% crosslinked P(St-*co*-O-B-EG600) nanospheres was constructed from highly compacted polymer nanospheres with Fe_3O_4 nanoparticles deposited on their surface. This result revealed that our approach could be used to fabricate seamless colloidosomes, which had potential in the application of small molecule encapsulation. A typical SEM image of a broken ternary hybrid colloidosome shown in Fig. 4E revealed a clearly porous structure in interior of the colloidosome. Unexpectedly, the porous structure in the colloidosomes was constructed by polymer and Fe_3O_4 nanoparticles instead of PSt nanospheres. Since the P(St-*co*-O-B-EG600) nanospheres were core crosslinked, most of the uncrosslinked amphiphilic P(O-B-EG600) component could be dissolved by DCM, while a small amount of P(O-B-EG600) polymer chains could be covalently attached to the crosslinked PSt nanospheres, thereby endowing the PSt nanospheres with certain hydrophilicity. In the formation process of the ternary hybrid colloidosomes, PSt nanospheres along with a certain amount of amphiphilic P(O-B-EG600) polymer chains move to the surface of the oil droplet to form a seamless shell and some P(O-B-EG600) polymer chains accompanied with a certain amount of hydrophobic Fe_3O_4 nanoparticles migrate into the core of the oil droplet to construct porous structure. We consider that the synergy between amphiphilic P(O-B-EG600) polymer chains and PSt nanospheres leads to the formation of these ternary hybrid colloidosomes.

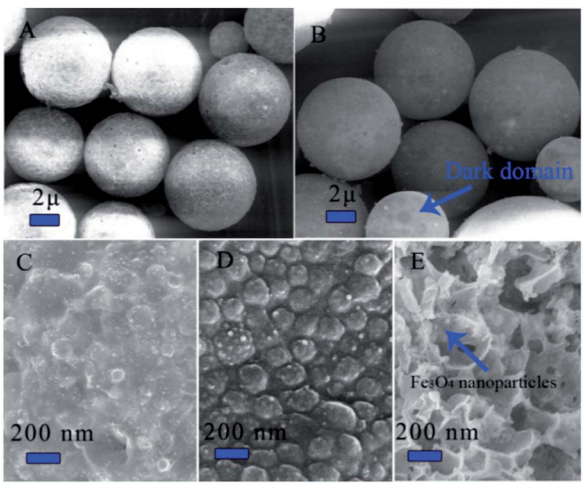

Fig. 4 SEM images of ternary hybrid colloidosomes generated by using P(St-*co*-O-B-EG600) nanoparticles crosslinked with (A) 5.0 and (B) 10.0 wt% of DVB while keeping the content of Fe_3O_4 nanoparticles at 15 wt%; (C) and (D) are the magnified SEM images of (A) and (B); (E) is the SEM image of the porous structure in interior of the colloidosomes.

3.3 Magnetic property and guest molecule encapsulation

Magnetic nanoparticles (MNPs) possess broad applications in many fields including drug delivery,[29–31] imaging[32–34] and separation system.[35,36] However, the prospects of the MNPs in these applications highly depend on the dispersion and long-time colloidal stability.[37] Surface modification[38,39] and carrier design[40,41] for the MNPs have been demonstrated to be promising methods to improve these two properties. Consequently, we were interested in testing whether our hybrid colloidosomes could bring a better dispersion to MNPs in the polymer matrix, thus increasing their magnetic properties. Fig. 5 shows the magnetic hysteresis loops of the polymer–Fe_3O_4 nanoparticle hybrid colloidosomes and polymer–polymer nanosphere–Fe_3O_4 nanoparticle ternary hybrid colloidosomes. Neither remanence nor coercivity was observed, revealing that these hybrid colloidosomes possessed superparamagnetic property. Polymer–Fe_3O_4 nanoparticle hybrid colloidosomes derived from 2.0, 4.0 and 8.0 L min^{-1} of airflow exhibited 2.6, 3.5 and 4.3 emu per g of saturation magnetizations, while polymer–polymer nanosphere–Fe_3O_4 nanoparticle ternary hybrid colloidosomes

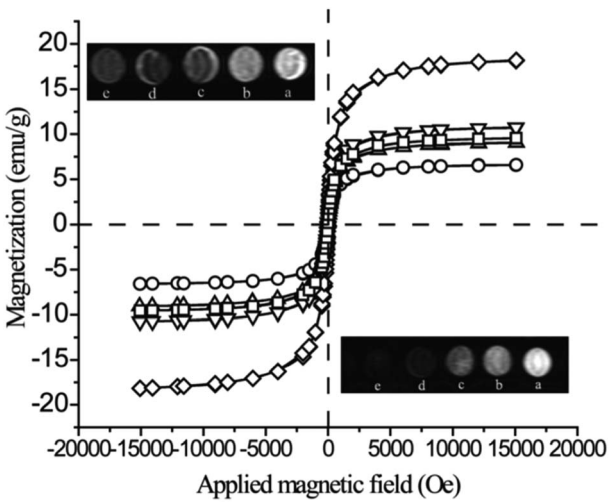

Fig. 5 Magnetic hysteresis loops of polymer–Fe_3O_4 nanoparticle hybrid colloidosomes prepared from 2.0 (○), 4.0(△) and 8.0 L min^{-1} (▽) airflow, and polymer–polymer nanosphere–Fe_3O_4 nanoparticle ternary hybrid colloidosomes generated by core crosslinked P(St-*co*-O-B-EG600) nanospheres with 5.0 wt% (□) and 10.0 wt% (◇) DVB crosslinker. The top and bottom insets are the MR images of polymer–Fe_3O_4 nanoparticle hybrid colloidosomes and polymer–polymer nanosphere–Fe_3O_4 nanoparticle ternary hybrid colloidosomes generated from P(St-*co*-O-B-EG600) nanospheres crosslinked with 10.0 wt% of DVB (airflow rate 4.0 L min^{-1}), the echo times are (a) 25, (b) 50, (c) 75, (d) 100 and (e) 125 ms.

prepared by using P(St-*co*-O-B-EG600) nanospheres crosslinked with 5.0 and 10.0 wt% DVB had 3.8 and 7.2 emu per g of saturation magnetizations. The actual magnetite contents (Table 1S†) calculated from these magnetic hysteresis loops were lower than the original feeding contents (15.0 wt%), which has already been demonstrated in previous reports.[42] Interestingly, evident discrepancy in magnetite content could be observed from the hybrid colloidosomes with different morphologies, though they were composed of similar feeding amount of Fe_3O_4 nanoparticles. Hybrid colloidosomes with hollow structures had a higher actual magnetite content (7.0 wt%) than that of the porous hybrid colloidosomes (4.2 and 5.7 wt%). Moreover, ternary hybrid colloidosomes exhibited much higher actual magnetite content than the polymer–Fe_3O_4 nanoparticle hybrid colloidosomes, with a highest actual magnetite content 11.7 wt%. These results implied that the encapsulation efficiency and dispersion of Fe_3O_4 nanoparticles in the polymer matrix depended much on the morphology of the hybrid colloidosomes. In the case of polymer–Fe_3O_4 nanoparticle hybrid colloidosomes, Fe_3O_4 nanoparticles could be well-dispersed in the shell of hollow hybrid colloidosomes (Fig. 3E and F), while the Fe_3O_4 nanoparticles were aggregated in interior of the porous hybrid colloidosomes (Fig. 3C and D). In the case of polymer–polymer nanosphere–Fe_3O_4 nanoparticle ternary hybrid colloidosomes, hydrophobic Fe_3O_4 nanoparticles were attached to the surface of hydrophobic PSt nanospheres, thus leading to a better loading and dispersion in the hybrid colloidosomes. Importantly, Fe_3O_4 nanoparticles were embedded in the shell of hollow hybrid colloidosomes (Fig. 3E) or attached to the surface of the PSt nanospheres in ternary hybrid colloidosomes (Fig. 4D) instead of being fully buried in the polymer matrix (such as the porous hybrid colloidosomes shown in Fig. 3C and D). As a result, Fe_3O_4 nanoparticles in hollow hybrid colloidosomes and ternary hybrid colloidosomes had a better moving capability, therefore making it easy for the magnetization direction of the Fe_3O_4 nanoparticles to be parallel.[28]

We expected that the Fe_3O_4 nanoparticles embedded in the colloidosomes could retain their favorable magnetic properties, thus endowing the hybrid colloidosomes promising potential as MRI contrast agents. Hollow hybrid colloidosomes and ternary hybrid colloidosomes were dispersed in deionized water, and then their MRI results were obtained from a varian MRI system. The top and bottom insets of Fig. 5 illustrate the T_2-weighted MR images of hollow polymer–Fe_3O_4 nanoparticle hybrid colloidosomes prepared from 8.0 L min^{-1} airflow rate and polymer–polymer nanosphere–Fe_3O_4 nanoparticle ternary hybrid colloidosomes generated with P(St-*co*-O-B-EG600) nanospheres crosslinked by 10.0 wt% of DVB (airflow rate 4.0 L min^{-1}), respectively. It was clear that Fe_3O_4 nanoparticles stabilized by ternary hybrid colloidosomes exhibited a much faster signal decay, which demonstrated a much shorter proton T_2 relaxation time.[43] To this end, we consider that the ternary hybrid colloidosomes may be a better MRI contrast agent than the polymer–Fe_3O_4 nanoparticle hybrid colloidosomes.

The aim of designing closed pore structure for these microspheres and colloidosomes was to realize a stable encapsulation of guest molecules. However, we also expected that this stabilization was tunable, thus the as encapsulated guests could be released in response to the environment stimuli. We used pyrene as a fluorescent probe to test the guest encapsulation and controllable release of the hybrid colloidosomes. The encapsulation process of pyrene into these capsules was described in details in the experimental section. We found that hydrophobic pyrene could be easily encapsulated in the hybrid colloidosomes by dissolving pyrene in DCM during the generation of these capsules. The encapsulation stability was tested by tracing the change of fluorescence spectra of pyrene at room temperature. A relatively slow decrease of fluorescence intensity of pyrene was observed (Fig. 6S†). This could be attributed to the precipitation of the hybrid colloidosomes, because of their large particle size. However, such a low decrease of fluorescence intensity after 24 h could still reveal a stable encapsulation.

In our previous work, we found that amphiphilic oligomer O-B-EG600 and crosslinked P(O-B-EG600) showed excellent thermal sensitivity at temperatures 33 and 41 °C, respectively.[26] We anticipated that the hybrid colloidosomes which contained the P(O-B-EG600) component might also exhibit morphology or property change under the stimulus of temperature variation, thereby leading to a controllable release of the encapsulated guest molecules. Indeed, we observed an evident release of pyrene from the hybrid colloidosomes at temperatures higher than 41 °C. The evolution of fluorescence emission spectra of pyrene encapsulated in the hybrid colloidosomes was shown in Fig. 7S.† All the characteristic peaks of pyrene exhibited synchronous decrease with the prolonging of time at 41 or 43 °C, indicating a significant decrease of pyrene retained in the solution. Since the release event was not observed at room temperature, we inferred that the as encapsulated pyrene was released from the hybrid colloidosomes and precipitated from the solution, because of its high hydrophobicity. Fig. 6A gives the release kinetics of pyrene from polymer–Fe_3O_4 nanoparticle hybrid colloidosomes (prepared by using 8.0 L min^{-1} airflow) and polymer–polymer nanosphere–Fe_3O_4 nanoparticle ternary hybrid colloidosomes (obtained from P(St-*co*-O-B-EG600) nanospheres crosslinked with 10.0 wt% DVB and 4.0 L min^{-1} airflow). Obviously, a higher temperature resulted in a faster release rate and a larger release extent, revealing that the release of pyrene was temperature dependent. Moreover, Fig. 6A also indicated that the release of pyrene from ternary hybrid colloidosomes was easier than polymer–Fe_3O_4 nanoparticle hybrid colloidosomes. This could be attributed to the polymer nanospheres, which brought a low packing intensity to the ternary hybrid colloidosomes, therefore making the deformation of the colloidosomes much easier.

To better understand the release mechanism of pyrene from the hybrid colloidosomes, we observed the morphology of the hybrid colloidosomes after the release of pyrene at 43 °C. As shown in SEM images Fig. 6B–E, an obvious morphology change was observed for both polymer–Fe_3O_4 nanoparticle hybrid colloidosomes and polymer–polymer nanosphere–Fe_3O_4 nanoparticle ternary hybrid colloidosomes. After the release of pyrene, these colloidosomes exhibited an open pore structure and deformed evidently. As the hybrid colloidosomes were stabilized by the outer layer composed of P(O-B-EG600), this

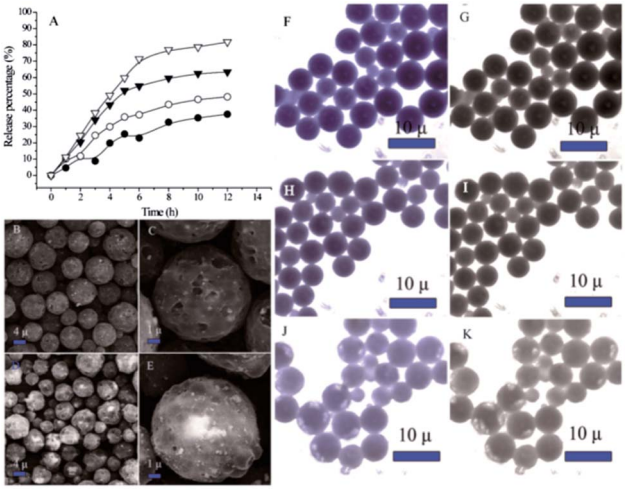

Fig. 6 (A) Pyrene release kinetics from polymer–Fe_3O_4 nanoparticle hybrid colloidosomes at 41 (●) and 43 °C (○), and polymer–polymer nanosphere–Fe_3O_4 nanoparticle ternary hybrid colloidosomes at 41 (▼) and 43 °C (▽); (B) and (C) are the overview and magnified SEM images of polymer–Fe_3O_4 nanoparticle hybrid colloidosomes after treating at temperature 43 °C for 12 h; (D) and (E) are the overview and magnified SEM images of polymer–polymer nanosphere–Fe_3O_4 nanoparticle ternary hybrid colloidosomes after treating at temperature 43 °C for 12 h; (F), (H) and (J) are the fluorescence microscope images of the ternary hybrid colloidosomes before and after emerging in the environment with 43 °C for 6 and 12 h, respectively; (G), (I) and (K) are the corresponding black-white photos of (F), (H) and (J), respectively.

thermal sensitive P(O-B-EG600) layer shrunk at high temperatures. As a result, the P(O-B-EG600) layer was destroyed by the driving force derived from its shrink, and the porous structure which was embedded under the P(O-B-EG600) layer was exposed. We consider that the morphology evolution of the hybrid colloidosomes from a closed pore structure to an open pore structure plays a key role in the temperature triggered release of pyrene (the shrink of the colloidosomes shown in Fig. 8S† confirmed this speculation). We also used an inverted fluorescence microscope to directly observe the release of pyrene from the ternary hybrid colloidosomes. Fig. 6F–K illustrate the fluorescence microscope images and corresponding black-white photos of the pyrene loaded ternary hybrid colloidosomes before and after treating at temperature 43 °C for 6 and 12 h. The blue color of the ternary hybrid colloidosomes faded significantly with the prolonging of treating time at 43 °C, indicating an evident release of pyrene. Consequently, it is reasonable to believe that these hybrid colloidosomes are promising capsules for the encapsulation and triggered release of guest molecules.

4. Conclusions

In conclusion, this paper has introduced a solvent evaporation assisted self-assembly route to polymer hollow microspheres and colloidosomes. The controllable airflow and the self-emulsification of the amphiphilic copolymer were the key factors, which led to the formation of closed pore structure. The obtained polymer microspheres, polymer–polymer nanosphere colloidosomes and polymer–Fe_3O_4 nanoparticle hybrid colloidosomes exhibited diameters around 10.0 μm and their interior pore structure could be controlled by simply adjusting the airflow rate. The dispersion of Fe_3O_4 nanoparticles in polymer–polymer nanosphere–Fe_3O_4 nanoparticle ternary hybrid colloidosomes was better than in polymer–Fe_3O_4 nanoparticle hybrid colloidosomes, thus making the ternary hybrid colloidosomes more promising as MRI contrast agent. Thanks to the excellent temperature sensitivity of the P(O-B-EG600) component, both hybrid colloidosomes and ternary hybrid colloidosomes changed from a closed pore structure to an open pore structure at temperatures around or higher than 41 °C. Therefore, the guest molecules encapsulated in the hybrid colloidosomes could be released under the stimulus of temperature change. We envisioned that this airflow-controlled solvent evaporation method might prove to be a green, simple and large-scale route to the generation of microcapsules. In combination of magnetic property and temperature sensitivity, we considered that these hybrid colloidosomes would be interesting in catalyst loading, drug encapsulation and controlled release.

Acknowledgements

This work was supported by the National Natural Science Foundation of China (51173153, U1205113, 51103122); the Scientific and Technical Project of Fujian Province of China (2009J1009).

References

1 B. M. Discher and A. Eisenberg, *Science*, 1999, **284**, 1143.
2 R. Chen, D. J. G. Pearce, S. Fortuna, D. L. Cheung and S. A. F. Bon, *J. Am. Chem. Soc.*, 2011, **133**, 2151.
3 J. Song, J. Zhou and H. Duan, *J. Am. Chem. Soc.*, 2012, **134**, 13458.
4 S. Egli, M. G. Nussbaumer, V. Balasubramanian, M. Chami, N. Bruns, C. Palivan and W. Meier, *J. Am. Chem. Soc.*, 2011, **133**, 4476.
5 G.-Y. Liu, C.-J. Chen and J. Ji, *Soft Matter*, 2012, **8**, 8811.
6 G.-Y. Liu, L.-P. Lv, C.-J. Chen, X.-S. Liu, X.-F. Hu and J. Ji, *Soft Matter*, 2011, **7**, 6629.
7 A. D. Dinsmore, M. F. Hsu, M. G. Nikolaides, M. Marquez, A. R. Bausch and D. A. Weitz, *Science*, 2002, **298**, 1006.
8 X.-W. Xu, X.-M. Zhang, C. Liu, Y.-L. Yang, J.-W. Liu, H.-P. Cong, C.-H. Dong, X.-F. Ren and S.-H. Yu, *J. Am. Chem. Soc.*, 2013, **135**, 12928.
9 C. Yuan, Y. Xu, N. Jiang, G. Cheng, B. Xu, N. He and L. Dai, *Soft Matter*, 2011, **7**, 3366.
10 R. K. Shah, J.-W. Kim and D. A. Weitz, *Langmuir*, 2010, **26**, 1561.
11 S. J. Hsieh, C. Wang and C. Chen, *Macromolecules*, 2009, **42**, 4787.
12 F. Gao, Z. Su, P. Wang and G. Ma, *Langmuir*, 2009, **25**, 3832.
13 D. Hao, F. Gong, G. Hu, J. Lei, G. Ma and Z. Su, *Polymer*, 2009, **50**, 3188.
14 A. T. Poortinga, *Langmuir*, 2008, **24**, 1644.

15 X. D. He, X. W. Ge, H. R. Liu, M. Z. Wang and Z. C. Zhang, *Chem. Mater.*, 2005, **17**, 5891.
16 F. Gao, Z.-G. Su, P. Wang and G.-H. Ma, *Langmuir*, 2009, **25**, 3832.
17 S. H. Im, U. Y. Jeong and Y. Xia, *Nat. Mater.*, 2005, **9**, 671.
18 U. Y. Jeong, S. H. Im, P. H. C. Camargo, J. H. Kim and Y. Xia, *Langmuir*, 2007, **23**, 10968.
19 D. J. Pochan, Z. Chen, H. Cui, K. Hales, K. Qi and K. L. Wooley, *Science*, 2004, **306**, 94.
20 A. J. Khopade and F. Caruso, *Biomacromolecules*, 2002, **3**, 1154.
21 J. Li, H. Möhwald, Z. An and G. Lu, *Soft Matter*, 2005, **1**, 259.
22 S.-H. Kim, J. W. Shim and S.-M. Yang, *Angew. Chem., Int. Ed.*, 2011, **50**, 1171.
23 T. Watanabe, T. Ono and Y. Kimura, *Soft Matter*, 2011, **7**, 9894.
24 S. Abraham, Y. H. Park, J. K. Lee, C.-S. Ha and I. Kim, *Adv. Mater.*, 2008, **20**, 2177.
25 S.-H. Kim and D. A. Weitz, *Angew. Chem., Int. Ed.*, 2011, **50**, 8731.
26 C. H. Yuan, Y. T. Xu, Y. M. Deng, J. F. Chen, Y. L. Liu and L. Z. Dai, *Soft Matter*, 2009, **5**, 4642.
27 C. Yuan, W. Luo, L. Zhong, H. Deng, J. Liu, Y. Xu and L. Dai, *Angew. Chem., Int. Ed.*, 2011, **50**, 3515.
28 L. Cui, H. Xu, P. He, K. Sumitomo, Y. Yamaguchi and H. Gu, *J. Polym. Sci., Part A: Polym. Chem.*, 2007, **45**, 5285.
29 K. Cheng, S. Peng, C. Xu and S. Sun, *J. Am. Chem. Soc.*, 2009, **131**, 10637.
30 H. Wu, S. Zhang, J. Zhang, G. Liu, J. Shi, L. Zhang, X. Cui, M. Ruan, Q. He and W. Bu, *Adv. Funct. Mater.*, 2011, **21**, 1850.
31 G. Beaune, M. Levy, S. Neveu, F. Gazeau, C. Wilhelm and C. Ménager, *Soft Matter*, 2011, **7**, 6248.
32 J. Xie, G. Liu, H. S. Eden, H. Ai and X. Chen, *Acc. Chem. Res.*, 2011, **44**, 883.
33 K. Li, D. Ding, D. Huo, K.-Y. Pu, N. N. P. Thao, Y. Hu, Z. Li and B. Liu, *Adv. Funct. Mater.*, 2012, **22**, 3107.
34 H. J. Chung, H. Lee, K. H. Bae, Y. Lee, J. Park, S.-W. Cho, J. Y. Hwang, H. Park, R. Langer, D. Anderson and T. G. Park, *ACS Nano*, 2011, **5**, 4329.
35 M. Piazza, M. Colombo, I. Zanoni, F. Granucci, P. Tortora, J. Weiss, T. Gioannini, D. Prosperi and F. Peri, *Angew. Chem., Int. Ed.*, 2011, **50**, 622.
36 J. H. Clement, M. Schwalbe, N. Buske, K. Wagner, M. Schnabelrauch, P. Görnert, K. O. Kliche, K. Pachmann, W. Weitschies and K. Höffken, *J. Cancer Res. Clin. Oncol.*, 2006, **132**, 287.
37 T. Borase, T. Ninjbadgar, A. Kapetanakis, S. Roche, R. O'Connor, C. Kerskens, A. Heise and D. F. Brougham, *Angew. Chem., Int. Ed.*, 2013, **52**, 3164.
38 K. El-Boubbou, D. C. Zhu, C. Vasileiou, B. Borhan, D. Prosperi, W. Li and X. Huanga, *J. Am. Chem. Soc.*, 2010, **132**, 4490.
39 L. Lartigue, C. Innocenti, T. Kalaivani, A. Awwad, M. Sanchez Duque, Y. Guari, J. Larionova, C. Guerin, J. G. Montero, V. Barragan-Montero, P. Arosio, A. Lascialfari, D. Gatteschi and C. Sangregorio, *J. Am. Chem. Soc.*, 2011, **133**, 10459.
40 Y. Deng, D. Qi, C. Deng, X. Zhang and D. Zhao, *J. Am. Chem. Soc.*, 2008, **130**, 28.
41 T. Zhang, J. Ge, Y. Hu, Q. Zhang, S. Aloni and Y. Yin, *Angew. Chem., Int. Ed.*, 2008, **47**, 5806.
42 H. Shang, W. S. Chang, S. Kan, S. A. Majetich and G. U. Lee, *Langmuir*, 2006, **22**, 2516.
43 F. Hu, L. Wei, Z. Zhou, Y. Ran, Z. Li and M. Gao, *Adv. Mater.*, 2006, **18**, 2553.